Catalysis Science & Technology

ROYAL SOCIETY OF CHEMISTRY

PAPER

View Article Online
View Journal | View Issue

Cite this: *Catal. Sci. Technol.*, 2025, **15**, 3613

Ceria-trapped single-atom rhodium catalysts for efficient ethanol steam reforming to hydrogen†

Lin Zhao,‡[ab] Diru Liu,‡[bc] Yiying Wang,[ab] Mengyuan Zhang,[bc] Qiang Wang, *[a] Guangyan Xu *[bc] and Hong He [bc]

Received 9th January 2025,
Accepted 7th May 2025

DOI: 10.1039/d5cy00025d

rsc.li/catalysis

Ethanol steam reforming (ESR) is a promising technique for sustainable hydrogen production, achieving high hydrogen yields. Herein, we prepare a series of Rh–Ce/Al_2O_3 catalysts with enhanced catalytic performance by modulating the interaction between active Rh and the CeO_2 promoter. Various characterization techniques, including HAADF-STEM and XAFS, demonstrated that new Rh–O–Ce sites were formed by the effective trapping of single-atom Rh species by CeO_2 nanoparticles on the Rh–Ce_5/Al_2O_3 catalyst. *In situ* DRIFTS-MS combined with isotopic kinetic analysis further revealed that Rh–O–Ce sites significantly enhanced water activation, which promoted the production of acetate, a reactive intermediate in ESR. Acetate was dehydrogenated to CO, which subsequently reacted with H_2O to form formate in the water–gas shift (WGS) reaction, a critical step in ESR. Similarly, the enhanced water activation also promoted the formation of formate, which ultimately decomposed to H_2 and CO_2. Consequently, the Rh–Ce_5/Al_2O_3 catalyst exhibited an excellent hydrogen production rate of 22.4 mmol g^{-1} min^{-1} at 450 °C and remarkable stability in the ESR reaction. The findings revealed the role of Rh–O–Ce sites in enhancing the performance of Rh-based catalysts in ESR, beneficial for the design of efficient ESR catalysts.

1. Introduction

Ethanol, a renewable biomass-derived compound with low toxicity and a favorable hydrogen-to-carbon ratio, represents an attractive material for hydrogen (H_2) production.[1–4] Ethanol steam reforming (ESR) has emerged as a pivotal technology for green H_2 generation, offering high H_2 yields while contributing to sustainable energy development.[2,5–7] Rh-based catalysts, with their exceptional ability to cleave C–C bonds and strong reforming activity, have proven to be among the most effective materials for ESR.[8–11] Despite their excellent catalytic properties, Rh-based catalysts still face several challenges in ESR, including poor H_2 selectivity due to the formation of by-products (*e.g.*, CH_4 and CO) and limited stability resulting from carbon deposition.[9,12–14] Numerous studies have been devoted to improving the H_2 production activity and stability of Rh-based catalysts in ESR by modulating the physical morphology and electronic structure of Rh.[15–18]

To address the above issues, for instance, Ito *et al.* developed Fe-promoted Rh/SiO_2 catalysts, which demonstrated improved H_2 selectivity and reduced carbon deposition by modulating the electronic environment of Rh through interaction with Fe oxide.[19] Similarly, Ferencz *et al.* provided a Rh–Co/CeO_2 catalyst, indicating that the synergistic effect of Rh and Co not only enhanced the reduction of cobalt and cerium oxides, but also effectively promoted the activation and conversion of ethanol molecules, and improved the selectivity to H_2 and the stability of the catalyst.[8] Recently, Meng *et al.* designed a novel 0.5RhNi/TiO_2 bimetallic catalyst in which the electron transferred from Ni to Rh and formed a multifunctional interface structure ($Rh–Ni^{\delta-}–O_v–Ti^{3+}$).[3] This catalyst achieved a remarkably high H_2 production at 400 °C, while significantly enhancing catalytic stability.[3] Overall, among the modification strategies, doping promoters has been recognized as an effective strategy to optimize both the physical morphology and electronic structure of Rh, thereby improving the activity and stability of Rh-based catalysts in ESR.[20–23]

Among the promoters, CeO_2 has proven to be an effective promoter with significant roles in controlling the Rh particle size and tuning its electronic structure.[24–26] Osorio-Vargas *et al.* developed a Rh/La_2O_3–CeO_2–γ-Al_2O_3 catalyst, demonstrating

[a] *College of Environmental Science and Engineering, Beijing Forestry University, Beijing 100083, China*
[b] *State Key Joint Laboratory of Environment Simulation and Pollution Control, Research Center for Eco-Environmental Sciences, Chinese Academy of Sciences, Beijing 100085, China. E-mail: gyxu@rcees.ac.cn*
[c] *University of Chinese Academy of Sciences, Beijing 100049, China*
† Electronic supplementary information (ESI) available. See DOI: **https://doi.org/10.1039/d5cy00025d**
‡ These authors contributed equally to this work.

that CeO_2 doping has reduced the Rh particle size and enhanced activity and stability.[24] Similarly, Zhu *et al.* designed a 2.0Rh5.0Ce–ZrO_2 catalyst, revealing that the introduction of Ce facilitated the formation of $Rh^{\delta+}$ active sites, thereby improving ethanol selectivity.[26] Additionally, CeO_2 can effectively promote the efficiency of the water–gas shift (WGS) reaction, a critical reaction step in ESR for enhancing H_2 production.[27–31] Zhurka *et al.* designed a Rh/CeO_2–ZrO_2–La_2O_3 catalyst by introducing CeO_2 into ZrO_2–La_2O_3, which promoted efficiently the WGS reaction, thereby significantly increasing the H_2 production of ESR.[32] Despite the well-established fact that CeO_2 doping enhances the activity of Rh-based catalysts in ESR, the nature of the structural interactions between Rh and Ce species and the underlying reaction mechanisms remain unclear.

In the present work, we designed and synthesized a series of Rh–Ce/Al_2O_3 catalysts to investigate the interaction mechanism between CeO_2 and Rh. These catalysts were thoroughly characterized using a variety of techniques, including X-ray diffraction (XRD), Brunauer–Emmett–Teller (BET), high angle annular dark field scanning transmission electron microscopy (HAADF-STEM), CO diffuse reflectance infrared Fourier transform spectroscopy (CO-DRIFTS), X-ray absorption fine structure (XAFS), X-ray photoelectron spectroscopy (XPS), and hydrogen temperature-programmed reduction (H_2-TPR). Furthermore, the reaction mechanism of ESR over Rh–Ce/Al_2O_3 catalysts was explored using *in situ* diffuse reflectance infrared Fourier transform spectroscopy with mass spectrometry (*in situ* DRIFTS-MS). Based on these results, this study elucidated the mechanism by which CeO_2 nanoparticles trap single-atom Rh to form Rh–O–Ce sites, thereby enhancing the catalytic performance of ESR, which provided valuable insights into the design of efficient catalysts for sustainable hydrogen production.

2. Experimental

2.1 Catalyst preparation

Rh–Ce/Al_2O_3 catalysts with a certain Rh content (1 wt%) and varying Ce contents (1, 3, 5, and 10 wt%) were prepared by an impregnation method. Firstly, a certain amount of rhodium nitrate ($Rh(NO_3)_3$) and cerium nitrate ($Ce(NO_3)\cdot 6H_2O$) were dissolved in deionized water to form a solution. Subsequently, 10 g of γ-Al_2O_3 (SASOL, SBa200) was added to the above solution and stirred to form a suspension. Then, the solution was transferred to a rotameter, and excess water was removed and the samples were dried in an oven at 80 °C overnight. Finally, the samples were calcined in a muffle furnace at 500 °C for 3 hours and further reduced in 10% H_2/N_2 at 400 °C for 3 hours. These samples were named as Rh–Ce_x/Al_2O_3, where x represents the Ce content. For comparison, a Ce_5/Al_2O_3 sample without Rh species was prepared by the same process.

2.2 Catalyst characterization

Powder XRD was conducted on a Bruker D8 Advance diffractometer with Cu Kα radiation (λ = 0.15406 nm), using a voltage of 40 kV and a current of 40 mA. Nitrogen adsorption was performed on a physical adsorption instrument (ASAP 2460, Micromeritics), and the specific surface area was calculated according to the BET method. HAADF-STEM was performed on a transmission electron microscope (JEM-ARM200F). H_2-TPR experiments were conducted on a chemisorption analyzer (Micromeritics AutoChem 2920 II) equipped with a thermal conductivity detector (TCD). The catalyst (100 mg) was pretreated in 10% O_2/He at 400 °C for 1 hour and then cooled to 30 °C. Subsequently, the sample was heated to 800 °C at a ramp rate of 10 °C min^{-1} in 10% H_2/Ar.[33]

XPS analysis was performed on an X-ray photoelectron spectrometer (AXIS Supra, Kratos Analytical Ltd.). The binding energies of all elements were corrected for energy shifts with C 1s (284.8 eV). XAFS spectra were recorded at the BL11B beamline of Shanghai Synchrotron Radiation Facility (SSRF). For energy calibration, rhodium foil was employed, establishing a reference at E_0 = 23 220 eV. The XAFS spectra were recorded at room temperature using a 4-channel silicon drift detector (SDD) Bruker 5040. Rh K-edge extended X-ray absorption fine structure (EXAFS) spectra were recorded in transmission mode. The spectra were processed and analyzed using the software codes Athena and Artemis.

2.3 Catalyst activity test

The catalytic tests of ESR were investigated in a fixed-bed reactor (inner diameter of 6 mm). Before tests, a 20 mg sample physically mixed with 80 mg quartz sand (40–60 mesh) was pretreated in 10% H_2/N_2 at 400 °C for 1 hour. A mixture of H_2O (or D_2O) and ethanol with a H_2O (or D_2O) to ethanol ratio of 8 was injected into the reaction system at a flow rate of 27.1 μL min^{-1}. The reactants mixed with N_2 (123 mL min^{-1}) were evaporated at 130 °C before entering the reactor. The reactants and products were analyzed on-line using a gas chromatograph (Agilent 8890 GC) equipped with FID and TCD detectors. The ethanol conversion, carbonaceous product yield and product production rate were calculated by the following equations (eqn (1)–(3)).

$$\text{Ethanol conversion}\ (\%) = \frac{F_{\text{EtOH,in}} - F_{\text{EtOH,out}}}{F_{\text{EtOH,in}}} \times 100\% \quad (1)$$

$$\text{Carbonaceous product yield}\ (\%) = \frac{F_c \times j}{2\ \times F_{\text{EtOH,in}}} \times 100\% \quad (2)$$

$$\text{Product production rate}\ \left(\text{mmol g}^{-1}\ \text{min}^{-1}\right) = \frac{X\ (\%) \times Q \times K}{M_{\text{cat}} \times V_{\text{m}}} \quad (3)$$

The catalytic test of WGS was investigated in the above fixed-bed reactor. Before the test, a 10 mg sample mixed with 90 mg quartz sand (40–60 mesh) was pretreated in 10% H_2/N_2 at 400 °C for 1 hour. The water was fed into the reaction system at a flow rate of 9.64 μL min^{-1}, while the 2% CO/N_2 gas mixture at a flow rate of 138 mL min^{-1}. The

reactants were evaporated at 130 °C before entering the reactor. The reactants and products were analyzed on-line using a gas chromatograph (Agilent 8890 GC) equipped with FID and TCD detectors. The CO reaction rate and product production rate were calculated by the following equations (eqn (4) and (5)).

$$\text{Product production rate}\left(\text{mmol g}^{-1}\ \text{min}^{-1}\right) = \frac{X\,(\%) \times Q}{M_{\text{cat}} \times V_{\text{m}}} \quad (4)$$

$$\text{CO reaction rate}\left(\text{mmol g}^{-1}\ \text{min}^{-1}\right) = \frac{\left(X_{\text{CO,in}}\,(\%) - X_{\text{CO,out}}\,(\%)\right) \times Q}{g \times V_{\text{m}}} \quad (5)$$

where $F_{\text{EtOH,in/out}}$ is the molar flow rate of ethanol at the inlet (outlet). F_{C} denotes the molar rate of carbon-containing products at the outlet, where j indicates the number of carbon atoms. X (%) represents the amount of gas product generated, $X_{\text{CO,in/out}}$ (%) is the amount of CO at the inlet (outlet), and Q and K are the total flow rate (150 mL min^{-1}) and volume expansion factor, respectively. M_{cat} is the mass of the catalyst and V_{m} is the gas volume constant (22.4 L mol^{-1}).

2.4 *In situ* DRIFTS-MS

CO-DRIFTS was carried out on a FTIR spectrometer (Nicolet IS 50) equipped with an MCT detector.[34] Spectra were obtained by accumulating 100 scans at a resolution of 4 cm^{-1}. Prior to testing, samples were reduced in H_2/Ar at 200 °C for 30 min. After pretreatment, the samples were cooled to 30 °C in Ar. CO adsorption was then carried out at 30 °C with 1% CO/Ar, and after saturation, the samples were purged with Ar for 30 min to remove the weakly adsorbed CO. The spectra of CO-DRIFTS were further collected.

In situ DRIFTS-MS experiments were performed on a FTIR spectrometer equipped with an on-line mass spectrometer (InProcess Instruments, GAM 200).[35] The spectra were collected with an accumulation of 100 scans at 4 cm^{-1} resolution, and the gaseous products (H_2: m/z = 2, CO_2: m/z = 44, CO: m/z = 28, CH_4: m/z = 15, H_2O: m/z = 17, C_2H_4: m/z = 26) were monitored by online MS. Before the test, the samples were reduced in H_2/Ar at 400 °C for 30 min. In the EtOH-TPD experiment, the samples were pre-exposed to 0.3% C_2H_5OH/Ar at 100 °C for 1 hour, followed by heating in Ar from 100 °C to 500 °C at a rate of 10 °C min^{-1}, with spectra collected every minute. During the ESR-TPSR experiment, the samples were exposed to 0.16% C_2H_5OH/1.3% H_2O/Ar and heated from 100 °C to 500 °C at a rate of 10 °C min^{-1}. During the step-response experiments of CH_3COOH, the samples were exposed to 0.075% CH_3COOH/Ar for 30 min, then Ar for 30 min, and finally 0.75% H_2O/Ar for 60 min at 350 °C. During the WGS-TPSR experiment, the samples were heated in 1% CO/1.2% H_2O/Ar from 200 °C to 500 °C at a rate of 10 °C min^{-1}. During the step-response experiments of CO, the samples were exposed to 1% CO/Ar for 30 min, then Ar for 30 min, and finally 1.2% H_2O/Ar for 60 min at 200 °C.

3. Results and discussion

The physical and chemical properties of the Rh–Ce/Al_2O_3 catalysts were systematically characterized using various methods. XRD patterns showed that diffraction peaks (2θ = 31.9°, 37.6°, 39.5°, 45.8°, 60.9°, 66.8°) corresponding to the γ-Al_2O_3 phase (JCPDS no. 02-1420) were present in all the catalysts (Fig. 1a).[33] In contrast, Rh species were hardly observed on Rh/Al_2O_3, suggesting the high dispersion of Rh species.[36] Similarly, Rh species, as well as CeO_2 species, were not observed on Rh–Ce_1/Al_2O_3. As the Ce content increased, characteristic peaks (2θ = 28.6°, 33.1°, 56.3°) due to CeO_2 (JCPDS no. 34-0394) gradually emerged and enhanced on the Rh–Ce_x/Al_2O_3 samples ($x \geq 3$).[37] In addition, characteristic peaks of CeO_2 were also observed on Ce_5/Al_2O_3 (Fig. S1†). BET analysis showed that Rh loading did not affect the specific surface area of Rh/Al_2O_3 (190 $\text{m}^2\ \text{g}^{-1}$), while increased Ce loading induced a gradual decrease in the specific surface area of the Rh–Ce_x/Al_2O_3 catalysts, possibly due to the coverage of CeO_2 on the Al_2O_3 surface (Table 1).[24] Besides, the specific surface area of Ce_5/Al_2O_3 was similar to that of Rh–Ce_5/Al_2O_3.

HAADF-STEM images and energy dispersive spectroscopy (EDS) showed that small Rh nanoclusters with an average particle size of 1.23 nm were present on Rh/Al_2O_3 (Fig. 1b and S2†). Upon the introduction of a small amount of Ce, Rh nanoclusters with a slightly smaller average size of 0.93 nm were still observed on Rh–Ce_1/Al_2O_3, accompanied by some highly dispersed Ce atoms (Fig. 1c and S3†).[38] As the Ce loading increased, Rh nanoparticles were hardly observed on Rh–Ce_3/Al_2O_3, while small CeO_2 nanoparticles (2.03 nm) emerged (Fig. S4†). Meanwhile, around the CeO_2 nanoparticles, a certain amount of highly dispersed single-atom Rh could be detected. Notably, as the Ce loading further increased, larger CeO_2 nanoparticles (4.83 nm) were observed on Rh–Ce_5/Al_2O_3, accompanied by a large amount of highly dispersed single-atom Rh (Fig. 1d and S5†). EDS analysis further showed that single-atom Rh species were predominantly located around CeO_2 nanoparticles, indicating the effective trapping of single-atom Rh by CeO_2 nanoparticles (Fig. 1e). These results demonstrated that highly dispersed Ce atoms alone did not significantly change the physical state of Rh species. However, when small CeO_2 nanoparticles formed, they began to interact with Rh, promoting the dispersion of Rh species. Furthermore, when the content of Ce was further increased, large CeO_2 nanoparticles would be formed and facilitated the substantial trapping of single-atom Rh.

The *in situ* DRIFTS experiment of CO adsorption showed that several bonds due to geminal-dicarbonyl CO adsorption (2088 cm^{-1} and 2012 cm^{-1}) on highly dispersed Rh atoms and linear- (2058 cm^{-1}) and bridge-bonded (1833 cm^{-1}) CO adsorption on Rh nanoparticles were observed on Rh/Al_2O_3 (Fig. 1f).[18,39,40] The introduction of a small amount of CeO_2 only slightly changed CO adsorption on Rh–Ce_1/Al_2O_3, suggesting a similar Rh state to the Rh/Al_2O_3 sample. In

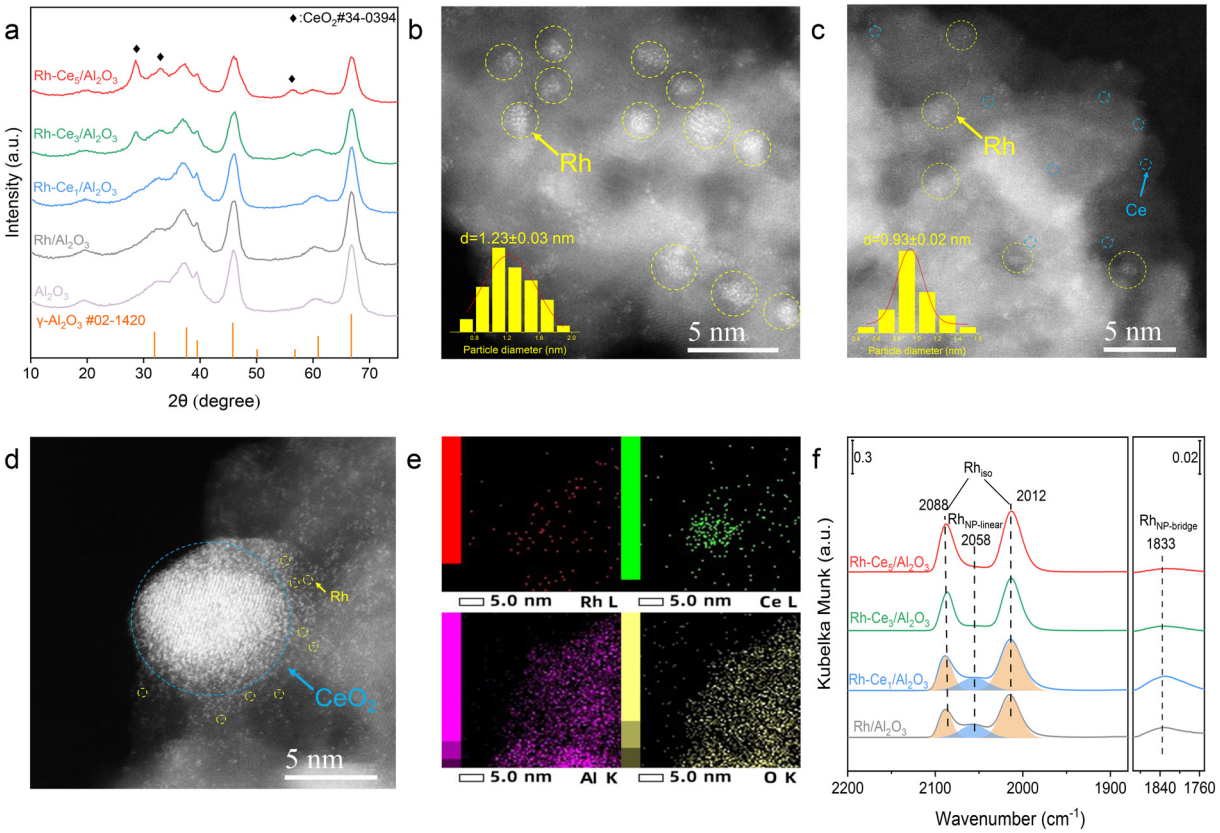

Fig. 1 (a) XRD patterns of Rh–Ce_x/Al_2O_3 catalysts. HAADF-STEM images and particle size statistics (inset) of (b) Rh/Al_2O_3 and (c) Rh–Ce_1/Al_2O_3. HAADF-STEM image (d) and the corresponding elemental mapping (e) of Rh–Ce_5/Al_2O_3. (f) CO-DRIFTS spectra of the Rh–Ce_x/Al_2O_3 catalysts.

contrast, only the bands at 2088 cm^{-1} and 2012 cm^{-1}, assigned to CO adsorption on single-atom Rh, were observed on Rh–Ce_5/Al_2O_3. Additionally, the increased band signals for Rh single atoms further confirmed that large CeO_2 nanoparticles efficiently trapped single-atom Rh, consistent with the HAADF-STEM images.[41]

The electronic states and local structures of Rh species on Rh–Ce_x/Al_2O_3 were further characterized by XAFS. In the X-ray absorption near edge spectroscopy (XANES) analysis, compared to the Rh foil, the absorption edges of Rh/Al_2O_3, Rh–Ce_3/Al_2O_3 and Rh–Ce_5/Al_2O_3 shifted to higher energy with varying degrees, indicating that the Rh species were in different degrees of oxidized state (Fig. 2a). Among them, the shift of the Rh/Al_2O_3 absorption edge toward a higher energy was slight, suggesting that Rh species were primarily in the oxidized state with a small fraction in the metallic state. In contrast, the introduction of CeO_2 caused the absorption edge of Rh–Ce_3/Al_2O_3 to shift to a higher energy compared to Rh/Al_2O_3. Notably, as the Ce content increased, the shift of the Rh–Ce_5/Al_2O_3 absorption edge toward a higher energy was pronounced compared to both Rh/Al_2O_3 and Rh–Ce_3/Al_2O_3, and the absorption edge of Rh–Ce_5/Al_2O_3 was closer to that of Rh_2O_3, indicating that the Rh species were predominantly in the oxidized state of +3. This progressive shift indicated that the introduction of CeO_2 with increasing content had an effect of increasing the oxidation state of Rh species.[42] In the extended X-ray absorption fine structure (EXAFS) analysis, on Rh/Al_2O_3, the bands at 1.5 Å and 2.4 Å assigned to Rh–O and Rh–Rh bonds were observed, respectively, further indicating that the Rh species were primarily oxidized, with some metallic Rh nanoclusters present (Fig. 2b).[18] However, one band corresponding to Rh–O bonds and a new weak band at 2.6 Å, assigned to Rh–O–Ce bonds,[43] were observed on Rh–Ce_3/Al_2O_3, without any Rh–Rh or Rh–O–Rh bonds detected, indicating the dispersion of Rh as single atoms in Rh–Ce_3/Al_2O_3.[18,42,44] On Rh–Ce_5/Al_2O_3, the intensity of the Rh–O–Ce bond increased, further confirming that CeO_2 led to the formation of a unique Rh–O–Ce coordination structure, which likely facilitated the single atom dispersion of Rh species. Additionally, in the wavelet transform (WT) spectra, both

Table 1 Physical and chemical properties of Rh–Ce/Al_2O_3 catalysts

Catalyst	Surface area ($m^2\ g^{-1}$)	H_2 consumption (μmol g^{-1})		XPS percentage (%)		
		Rh^{3+} to Rh^0	Ce^{4+} to Ce^{3+}	Rh^{3+}	Ce^{3+}	O_s
Al_2O_3	194	—	—	—	—	4.5
Rh/Al_2O_3	190	140	—	91	—	6.2
Rh–Ce_1/Al_2O_3	189	145	—	94	91.4	6.4
Rh–Ce_3/Al_2O_3	185	135	51	100	45.2	8.4
Rh–Ce_5/Al_2O_3	176	139	63	100	29.0	10.7
Ce_5/Al_2O_3	178	—	133	—	32.5	9.9

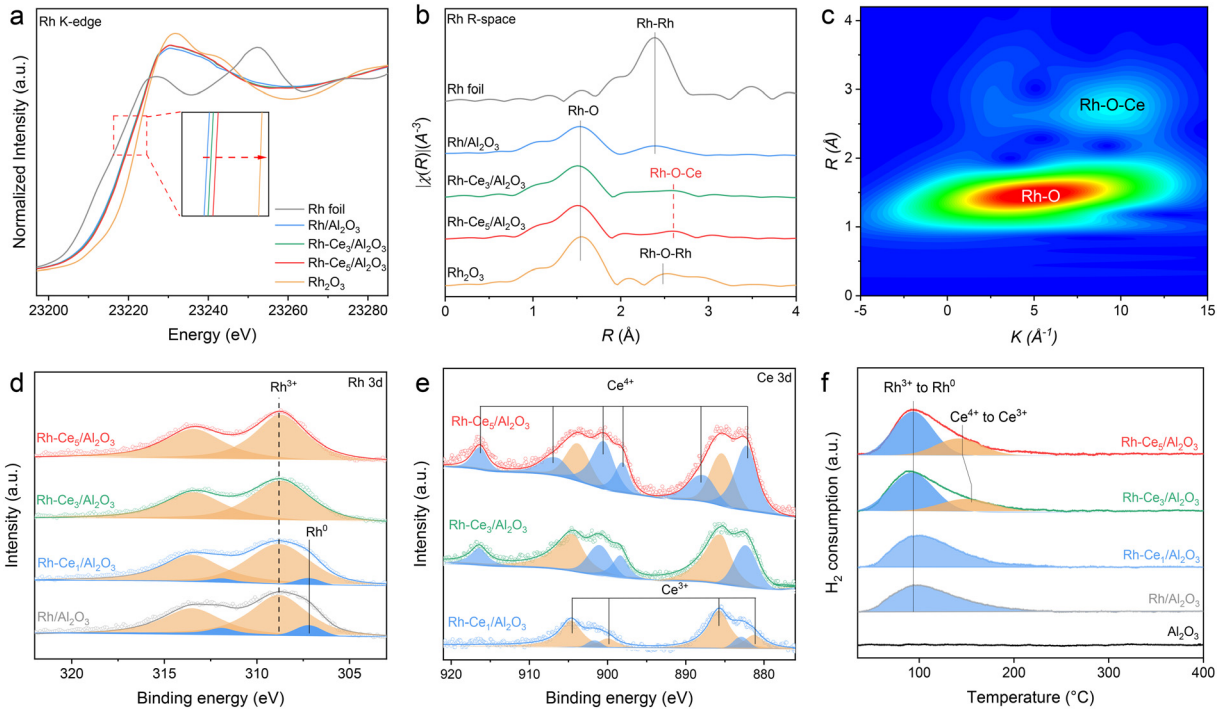

Fig. 2 (a) XANES spectra of the Rh K-edge for Rh–Ce_x/Al_2O_3 catalysts, with an inset showing an enlarged view of the absorption edge. (b) EXAFS spectra of Rh–Ce_x/Al_2O_3 catalysts. (c) The WT spectroscopy of Rh–Ce_5/Al_2O_3. (d) Rh 3d XPS spectra of Rh–Ce_x/Al_2O_3. (e) Ce 3d XPS spectra of Rh–Ce_x/Al_2O_3, and (f) H_2-TPR profiles of Al_2O_3 and Rh–Ce_x/Al_2O_3.

Rh–O bonds and Rh–Rh bonds were observed on Rh/Al_2O_3 (Fig. S6†). Conversely, on Rh–Ce_3/Al_2O_3 and Rh–Ce_5/Al_2O_3, only Rh–O and Rh–O–Ce bonds with increasing intensity were detected, while no Rh–Rh or Rh–O–Rh bonds were observed (Fig. 2c and S6†). Meanwhile, the fitting results from FT k^3-weighted Fourier transforms of the EXAFS (Fig. S7†) showed that Rh in Rh–Ce_5/Al_2O_3 is primarily coordinated to oxygen atoms in the first coordination shell, with an average Rh–O bond distance of 1.7 Å and a coordination number of 5.6. Additionally, a second coordination shell was observed, corresponding to Rh–O–Ce interactions, with an average Rh–O–Ce bond distance of 2.8 Å and a coordination number of 1.5. The XAFS results confirmed the trapping of single-atom Rh by CeO_2 nanoparticles and thus the formation of the new Rh–O–Ce structure, consistent with observations from HAADF-STEM imaging.

Subsequently, these samples were analyzed by using the XPS technique. On the Rh–Ce/Al_2O_3 catalysts, the Rh 3d spectra were deconvoluted into four peaks, attributed to Rh^0 (307.2 and 311.9 eV) and Rh^{3+} (313.5 and 308.8 eV), respectively (Fig. 2d).[40,45–47] A small amount of metallic Rh^0 was observed on Rh/Al_2O_3 (9%) and Rh–Ce_1/Al_2O_3 (6%), while oxidized Rh^{3+} species (100%) were predominant on Rh–Ce_3/Al_2O_3 and Rh–Ce_5/Al_2O_3, suggesting that the Rh species on Rh–Ce_3/Al_2O_3 and Rh–Ce_5/Al_2O_3 were primarily oxidized, consistent with the results of XAFS. Concurrently, the Ce 3d spectra were deconvoluted into ten peaks (Fig. 2e), attributed to Ce^{3+} (881.1, 885.8, 899.8 and 904.7 eV) and Ce^{4+} (882.1, 888.1, 898.0, 900.6, 906.9 and 916.3 eV).[48–50] On Rh–Ce_1/Al_2O_3, Ce was primarily present as Ce^{3+} (91.4%). However, as the Ce content increased, the proportion of Ce^{3+} decreased significantly, while Ce^{4+} species dominated, increasing from 54.8% (Rh–Ce_3/Al_2O_3) to 71% (Rh–Ce_5/Al_2O_3), possibly due to the progressive formation of CeO_2 nanoparticles. The same result was also observed for Ce_5/Al_2O_3 (Fig. S9a†), where Ce^{4+} accounted for 67.5%. The valence band XPS spectra (Fig. S8†) showed no significant differences between Rh/Al_2O_3 and Rh–Ce_5/Al_2O_3, indicating that the electronic structure near the Fermi level was not significantly altered by the presence of CeO_2. Furthermore, Rh–Ce_5/Al_2O_3 was further tested at two different reaction temperatures (400 °C and 600 °C) in the ESR reaction, which produced poor H_2 conditions of 4% H_2 concentration and rich H_2 conditions with 10% H_2 concentration, respectively, and the reacted samples were analyzed by XPS (Fig. S10†). The binding energy of Rh^{3+} and the amount of Ce^{3+} did not change significantly under these two reaction conditions, respectively, indicating that the Rh–O–Ce structure remained highly stable under reaction conditions. The O 1s spectra were deconvoluted into two peaks (Fig. S9b†), attributed to the lattice oxygen (531.1 eV) and the surface oxygen (533.1 eV).[51] The surface oxygen proportion was 4.5%, and the lattice oxygen accounting for the majority was observed on Al_2O_3. The surface oxygen content of Rh/Al_2O_3 and Rh–Ce_1/Al_2O_3 was 6.2% and 6.4%, respectively. With further increase in Ce loading, the surface oxygen content gradually increased from 8.4% (Rh–Ce_3/Al_2O_3) to 10.7% (Rh–Ce_5/Al_2O_3), mainly due to oxygen species in CeO_2 nanoparticles.[51] Notably, a significant linear relationship between the oxygen vacancy content and single-atom Rh content further indicated a stabilizing effect of

oxygen vacancies on Rh single atoms on the CeO_2 surface (Fig. S11†).

H_2-TPR experiments were conducted to elucidate the redox properties of Rh and Ce species on these samples (Fig. 2f and Table 1). No H_2 consumption was detected on Al_2O_3, while a H_2 consumption peak at 350 °C (133 μmol g^{-1}), corresponding to the reduction of surface Ce^{4+} to Ce^{3+}, was observed on Ce_5/Al_2O_3 (Fig. S12†). On Rh/Al_2O_3, a H_2 consumption peak at 96 °C (140 μmol g^{-1}) was observed, attributed to the reduction of Rh^{3+} to Rh^0, consistent with the theoretical H_2 consumption for the complete reduction of all Rh^{3+} species (144 μmol g^{-1}).[52] A similar H_2 consumption for the reduction of Rh^{3+} to Rh^0 was observed for all Rh–Ce_x/Al_2O_3 samples. Only a single H_2 consumption peak at 96 °C (145 μmol g^{-1}) was observed on $Rh–Ce_1/Al_2O_3$, indicating that highly dispersed Ce atoms did not change the redox properties of Rh species. In contrast, a new H_2 consumption peak (51 μmol g^{-1}) located at 147 °C attributed to the reduction of Ce^{4+} to Ce^{3+} was observed on $Rh–Ce_3/Al_2O_3$, which was likely due to H_2 spillover on Rh–O–Ce. Further, this reduction peak shifted to a lower temperature (133 °C) with a greater H_2 consumption (63 μmol g^{-1}) on the $Rh–Ce_5/Al_2O_3$ sample, further confirming the formation of the Rh–O–Ce structure facilitating H_2 spillover.

In the ESR reaction, Al_2O_3 and Ce_5/Al_2O_3 were inactive for H_2 production, indicating that the introduction of Ce alone did not enhance this activity (Fig. S13b†). Rh/Al_2O_3 achieved 89% ethanol conversion at 400 °C. However, the Rh–Ce_x/Al_2O_3 (x = 1, 3, 5, 10) catalysts showed almost complete conversion of ethanol at the same temperature (Fig. S13a†). Rh/Al_2O_3 achieved an ethanol conversion of 98% at 450 °C, accompanied by a low CO_2 yield (21.3%) and a high CO yield (44.2%), along with a poor carbon balance (87.8%), likely due to carbon deposition on the catalyst surface (Fig. 3a). In

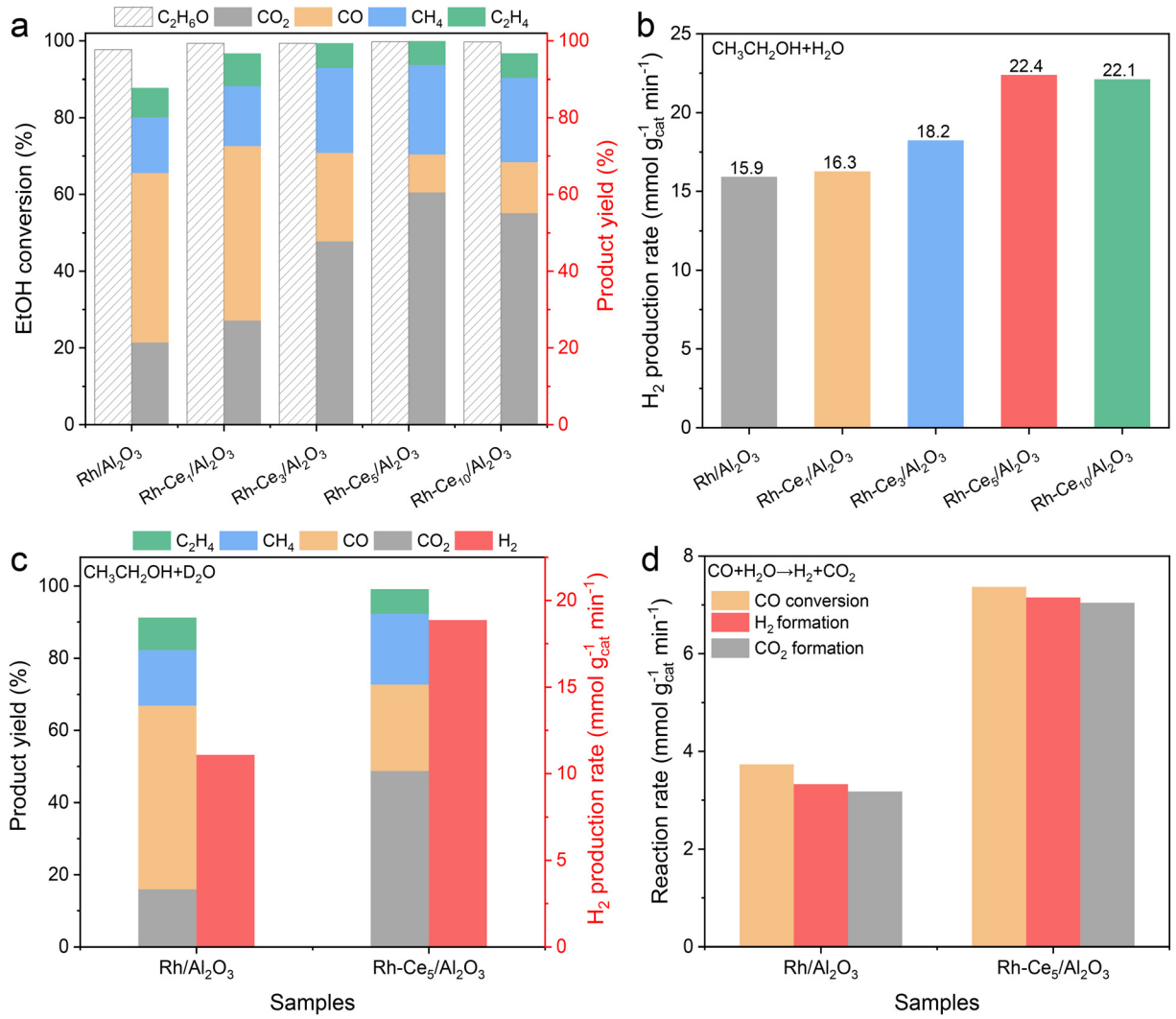

Fig. 3 (a) Ethanol conversion, carbon product yield, and (b) H_2 production rate over Rh–Ce_x/Al_2O_3 catalysts during the ESR reaction (reaction conditions: liquid feed of H_2O/ethanol = 8 at 27.1 μL min^{-1}, with balance N_2 at 123 mL min^{-1}, 20 mg catalyst and 80 mg SiO_2, 450 °C). (c) Ethanol and D_2O steam reforming of Rh/Al_2O_3 and $Rh–Ce_5/Al_2O_3$ (reaction conditions: liquid feed of D_2O/ethanol = 8 at 27.1 μL min^{-1} with balance N_2 at 123 mL min^{-1}, 20 mg catalyst and 80 mg SiO_2, 450 °C). (d) WGS reaction of Rh/Al_2O_3 and $Rh–Ce_5/Al_2O_3$ (reaction conditions: liquid feed of H_2O at 9.64 μL min^{-1}, the gas flow rate of CO is 3 mL min^{-1}, with balance N_2 at 135 mL min^{-1}, 10 mg catalyst and 90 mg SiO_2, 400 °C).

contrast, the Rh–Ce_x/Al_2O_3 catalysts achieved an excellent carbon balance at 450 °C, probably because the reactive oxygen species on CeO_x reduced carbon deposition.[53] However, significant differences were observed in the distribution of gaseous products (CO_2, CO, CH_4, and H_2). Rh–Ce_1/Al_2O_3 displayed a similar product distribution to Rh/Al_2O_3, with a low CO_2 yield (27.1%) and a high CO yield (45.5%). As the Ce loading increased, the CO production gradually decreased, while the yields of CO_2 (47.8%) and CH_4 (22.1%) increased on Rh–Ce_3/Al_2O_3. The lowest CO yield (9.9%) and the highest CO_2 yield (60.5%) were observed on Rh–Ce_5/Al_2O_3. The H_2 production rate gradually increased on the Rh–CeO_2/Al_2O_3 catalysts with increasing Ce content (Fig. 2b). Compared to Rh/Al_2O_3 (15.9 mmol g^{-1} min^{-1}), the H_2 production rate on Rh–Ce_1/Al_2O_3 increased very weakly (16.3 mmol g^{-1} min^{-1}), which indicated that the highly dispersed Ce atoms did not improve the H_2 production. In contrast, Rh–Ce_5/Al_2O_3 showed the maximum H_2 production rate (22.4 mmol g^{-1} min^{-1}), demonstrating to be an efficient ESR catalyst compared to other reported Rh-based catalysts (Table S1†). In addition, during the stability test (Fig. S15†), the ethanol conversion rate of Rh/Al_2O_3 dropped sharply from 100% to 50% after 100 hours, while the H_2 production rate decreased significantly from 20 mmol g^{-1} min^{-1} to 5 mmol g^{-1} min^{-1}. In contrast, the Rh–Ce_5/Al_2O_3 catalyst maintained a high ethanol conversion (99%) and H_2 production rate (36 mmol g^{-1} min^{-1}) in the first 50 hours, after which they began to decrease gradually to 60% and 22 mmol g^{-1} min^{-1}, respectively, in the next 50 hours. Furthermore, Raman experiments were conducted to characterize the carbon species deposited on the Rh/Al_2O_3 and Rh–Ce_5/Al_2O_3 catalysts after 1, 24, and 100 h of ESR reaction at 450 °C (Fig. S16†). On Rh/Al_2O_3 after 1 h of ESR reaction, the D-band at 1332 cm^{-1}, attributed to amorphous carbon, and the G-band at 1598 cm^{-1}, attributed to graphitic carbon, were observed.[54] The ratio of the peak areas of the D and G bands (I_G/I_D) was 0.65, indicating that the carbon deposition was mainly amorphous carbon. After 100 h of ESR reaction, the carbon deposition on Rh/Al_2O_3 continued to accumulate. In contrast, no obvious peaks related to carbon deposition appeared for Rh–Ce_5/Al_2O_3 after 1 h and 24 h, and the peak intensity of carbon on Rh–Ce_5/Al_2O_3 was still much lower than that on Rh/Al_2O_3 after 100 h. These results suggested that the carbon deposition may be an important reason for the rapid deactivation of Rh/Al_2O_3, and that the introduction of Ce effectively inhibited the carbon deposition.

Water activation is an important factor in enhancing the performance of Rh catalysts in the ESR reaction.[25,55,56] To evaluate their activity in water activation, the Rh–Ce/Al_2O_3 catalysts were further tested in ethanol reforming with D_2O (Fig. 3c and S17†). Rh/Al_2O_3 reached 100% ethanol conversion, and the product distribution showed a high CO yield (50.9%) and a low CO_2 yield (15.9%), with a low H_2 production rate (11.1 mmol g^{-1} min^{-1}), indicating that water activation significantly impacted the catalytic performance of Rh/Al_2O_3. In contrast, Rh–Ce_5/Al_2O_3 also achieved 100% ethanol conversion, but the product distribution exhibited a higher CO_2 production (48.7%) and an improved H_2 production rate (18.9 mmol g^{-1} min^{-1}). Compared to the significantly decreased H_2 production on Rh/Al_2O_3 (from 15.9 mmol g^{-1} min^{-1} to 11.1 mmol g^{-1} min^{-1}), the slightly decreased H_2 production rate on Rh–Ce_5/Al_2O_3 (from 22.4 mmol g^{-1} min^{-1} in EtOH + H_2O to 18.9 mmol g^{-1} min^{-1} in EtOH + D_2O) suggested that the Rh–O–Ce structure enhanced the water activation efficiency. Moreover, as the water–gas shift reaction is a critical step in the ESR reaction, the Rh–Ce/Al_2O_3 catalysts were further tested in the WGS reaction at 400 °C (Fig. 3d).[3,8,57] Rh/Al_2O_3 demonstrated a poor activity in the WGS reaction with a relatively low CO conversion rate (3.7 mmol g^{-1} min^{-1}) and H_2 production rate (3.3 mmol g^{-1} min^{-1}). Conversely, Rh–Ce_5/Al_2O_3 exhibited a significantly higher CO conversion rate (7.3 mmol g^{-1} min^{-1}) and H_2 production rate (7.2 mmol g^{-1} min^{-1}). In summary, the Rh–O–Ce structure improved the catalytic performance of Rh–Ce_x/Al_2O_3 by enhancing water activation, as well as promoting the WGS reaction.

In situ DRIFTS-MS experiments were performed to elucidate the reaction mechanism of ESR on the Rh–Ce_5/Al_2O_3 catalyst. During ethanol TPD experiments, the formation of ethoxy species (2966 cm^{-1}, 2926 cm^{-1}, 2867 cm^{-1}),[3,12,58] accompanied by acetate species (1576 cm^{-1}, 1456 cm^{-1}, 1389 cm^{-1}),[58,59] was observed on Rh–Ce_5/Al_2O_3 at 100 °C (Fig. 4a). These findings suggested that the dissociative adsorption of ethanol generated ethoxy species, which were subsequently dehydrogenated and oxidized to form acetate.[40] As the temperature increased from 100 to 350 °C, the consumption of ethoxy and the accumulation of acetate were observed, alongside the initial production of CO at 200 °C. Simultaneously, the first production peaks of CO, CH_4, and H_2 at around 260 °C were observed by mass spectrometry, indicating that the decomposition of ethoxy and its dehydrogenation intermediate, acetaldehyde, to produce CO, CH_4 and H_2 might be the dominant pathway at this temperature (Fig. 4b).[12] As the temperature further increased from 350 to 500 °C, the acetate species were gradually consumed, accompanied by a decrease in CO production, which was likely due to the elevated temperature weakening the interaction between CO and the catalyst surface. Meanwhile, the second production peak of H_2 was observed at 390 °C concurrently with the generation of CO, suggesting that the decomposition of acetate to CO and H_2 was likely the major reaction occurring in this temperature range.[12,13] Additionally, a small amount of H_2O was detected due to dehydration of ethanol, which may participate in the WGS reaction to generate CO_2. These results showed that the decomposition of acetaldehyde and ethoxy produced some CO and a large amount of CH_4, whereas the decomposition of acetate produced only CO and negligible CH_4. Besides, significantly less acetate formation and lower CO and CH_4 production were observed on Rh/Al_2O_3 at low temperatures between 200 and 300 °C, suggesting a lower reactivity for

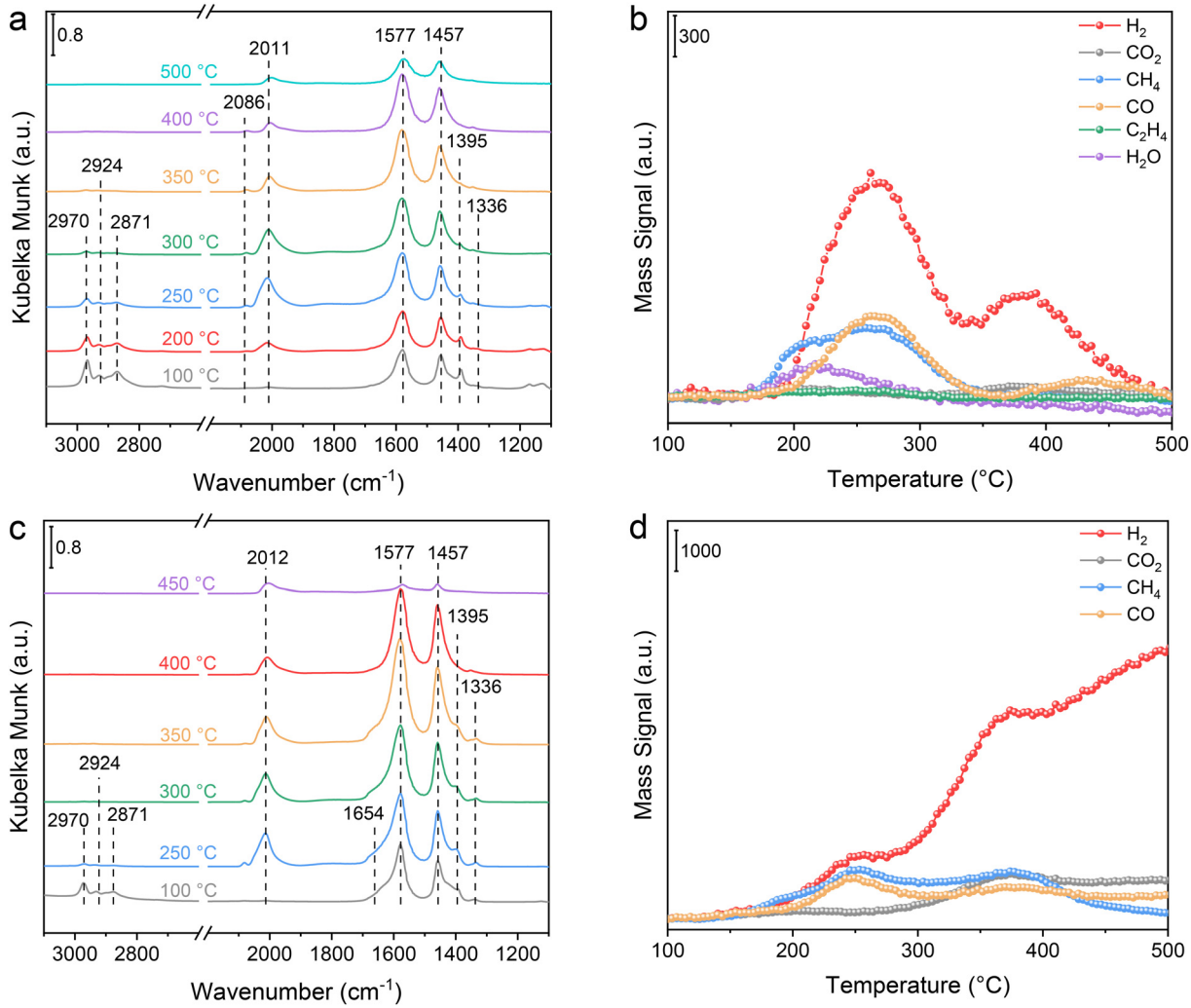

Fig. 4 (a) *In situ* DRIFTS spectra of the Rh–Ce_5/Al_2O_3 catalyst exposed to 0.3% CH_3CH_2OH/Ar. (b) The formation of H_2, CO_2, CH_4, CO, C_2H_4 and H_2O on Rh–Ce_5/Al_2O_3. (c) *In situ* DRIFTS spectra of surface intermediates on Rh–Ce_5/Al_2O_3 during the ESR reaction. (d) The formation of H_2, CO_2, CH_4 and CO during the ESR reaction.

ethoxy dehydrogenation to acetate on this catalyst (Fig. S18a†). At high temperatures between 300 and 500 °C, the consumption of acetate was also limited, accompanied by a lower H_2 production (Fig. S18b†). These findings demonstrated that the Rh–O–Ce structure facilitated the decomposition of ethoxy and its dehydrogenation product, acetaldehyde, producing CO and CH_4. Furthermore, the structure promoted the formation and subsequent consumption of acetate intermediates, leading to the production of additional CO and H_2.

During TPSR experiments of ESR, ethoxy species, acetate species, and the bending mode of water (between 1610 and 1670 cm^{-1}) were observed on Rh–Ce_5/Al_2O_3 at 100 °C (Fig. 4c).[12] As the temperature increased to 300 °C, the ethoxy species were consumed, accompanied by CO generation and an increase in acetate concentration. Concurrently, CO, CH_4, and H_2 production gradually increased, further indicating that the decomposition reaction of ethoxy and its dehydrogenation intermediate, acetaldehyde, predominantly occurred within this temperature range (Fig. 4d).[12] While the temperature increased to 350 °C, the ethoxy species were completely consumed, leading to the substantial production of CO and acetate. As the temperature further increased to 500 °C, the acetate species were progressively consumed, and the intensity of the CO peak decreased. Simultaneously, a notable increase in H_2 production was observed starting at 300 °C, along with CO_2 generation and a decrease in CO concentration, indicating the initiation of the WGS reaction. Within the temperature range of 300 to 500 °C, CO and CH_4 were still generated, though their formation was reduced compared to that below 300 °C. These observations further suggested that the continued decomposition of ethoxy and its dehydrogenated species acetaldehyde produced CH_4 and some CO.[13] Besides, on Rh/Al_2O_3, significantly less acetate formation and lower CO and CH_4 generation were observed as the temperature increased from 100 to 300 °C (Fig. S18c and d†). Furthermore, as the

temperature increased to 500 °C, the consumption of acetate was slight, accompanied by a reduced H_2 production, suggesting a lower reactivity of acetate intermediates on Rh/Al_2O_3. Notably, compared to Rh–Ce_5/Al_2O_3, CO_2 production began at higher temperatures (350 °C) and the concentration of CO_2 was relatively lower, indicating the poor WGS activity on Rh/Al_2O_3.[12,13,60] These demonstrated the crucial role of acetate as a reactive intermediate in the ESR reaction for H_2 production, while the Rh–O–Ce structure plays a pivotal role in facilitating the formation and consumption of the reactive intermediate acetate, as well as enhancing the efficiency of the WGS reaction. To further elucidate the role of acetate in the ESR reaction, step-response experiments of CH_3COOH were conducted. When Rh–Ce_5/Al_2O_3 was exposed to a CH_3COOH/Ar mixture at 350 °C, the formation of acetate species (1667, 1586, 1465, 1395, and 1328 cm^{-1})[12] was observed (Fig. 5a), while a large amount of CO was generated, indicating that CO may predominantly originate from the decomposition of acetate (Fig. 5c). After the removal of CH_3COOH, the intensity of acetate species showed only a slight change, indicating their strong adsorption on the catalyst surface (Fig. S19b†). However, the introduction of H_2O led to the rapid consumption of acetate within 20 min (Fig. 5b). Concurrently, the production of H_2 and CO_2 increased sharply within the first 10 min, reaching a maximum at approximately 5 min before gradually decreasing over the next 10 min (Fig. 5d). These observations confirmed that acetate served as an important intermediate, while acetate decomposed primarily to produce CO, which subsequently reacted with H_2O to generate CO_2. Additionally, when exposed to a CH_3COOH/Ar mixture at 350 °C, a lower amount of acetate species was observed on Rh/Al_2O_3, accompanied by lower CO generation (Fig. S19c†). Following the introduction of H_2O, the acetate consumption rate was considerably slower, with limited production of CO_2 and H_2 (Fig. S19d†). Overall, the Rh–O–Ce structure significantly enhanced water activation, thereby

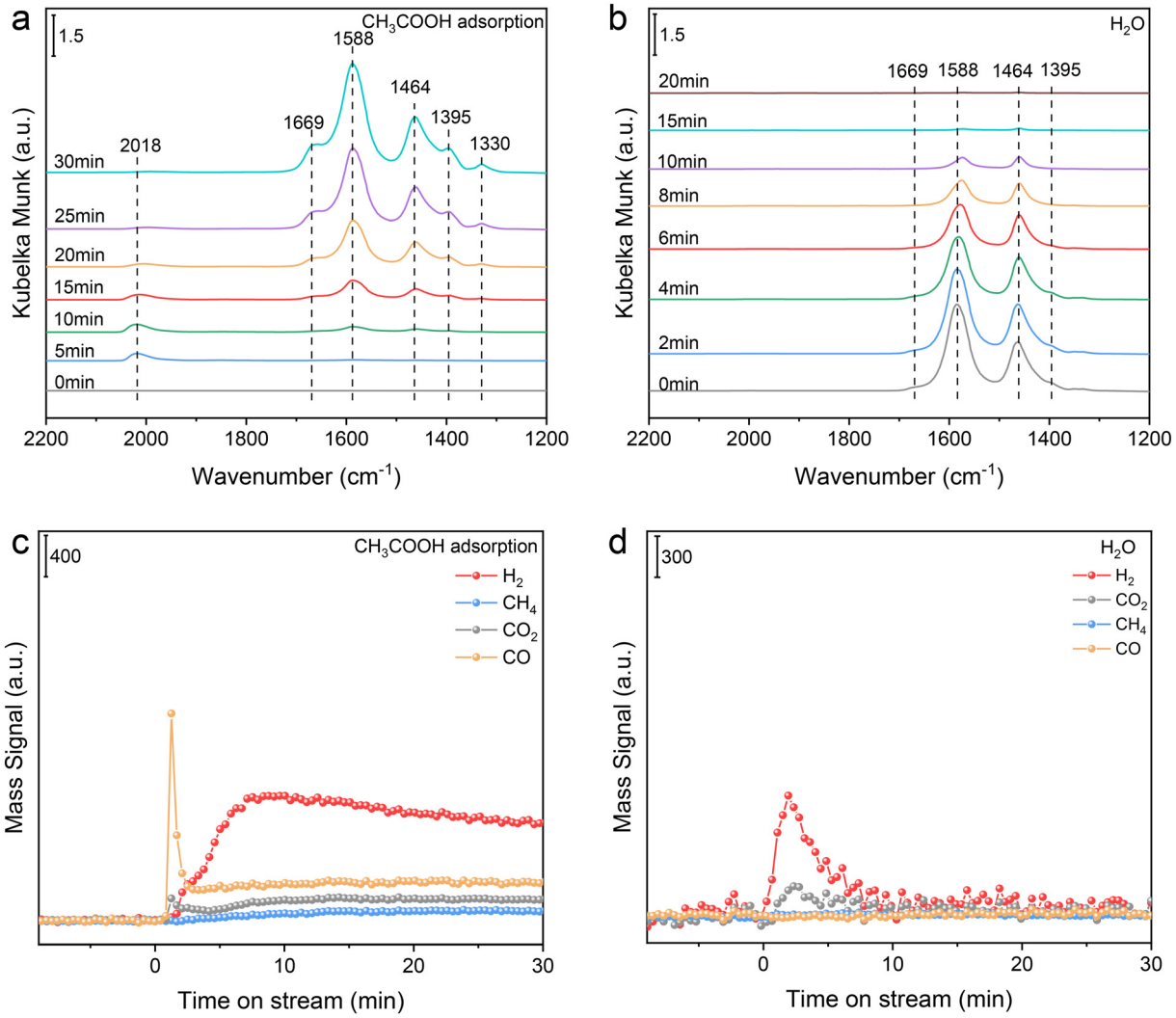

Fig. 5 *In situ* DRIFTS spectra of the Rh–Ce_5/Al_2O_3 catalyst exposed to (a) CH_3COOH/Ar and (b) H_2O at 350 °C. The formation of H_2, CO_2, CH_4 and CO on Rh–Ce_5/Al_2O_3 exposed to (c) CH_3COOH/Ar and (d) H_2O (rection conditions: pre-exposed to 0.075% CH_3COOH/Ar at 350 °C for 30 min, followed by Ar purging for 30 min, and finally exposed to 0.75% H_2O for 60 min).

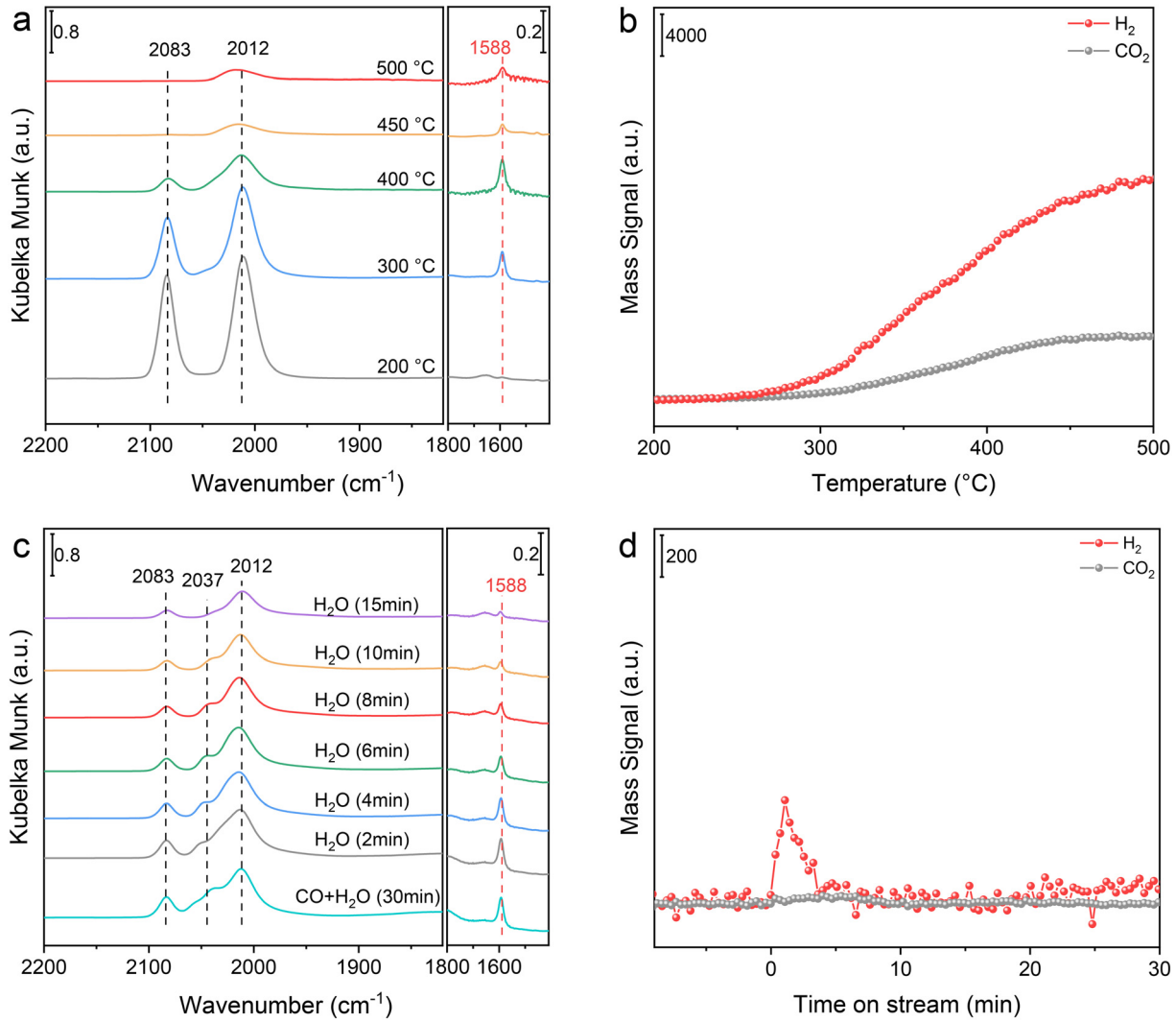

Fig. 6 (a) *In situ* DRIFTS spectra of surface intermediates on Rh–Ce_5/Al_2O_3 during the WGS reaction. (b) The formation of H_2 and CO_2 during the WGS reaction (reaction conditions: 1% CO/1.2% H_2O/Ar from 200 °C to 500 °C at a rate of 10 °C min^{-1}). (c) *In situ* DRIFTS spectra of the Rh–Ce_5/Al_2O_3 catalyst exposed to CO/H_2O/Ar and H_2O/Ar at 200 °C. (d) The formation of H_2 and CO_2 on Rh–Ce_5/Al_2O_3 exposed to H_2O/Ar (reaction conditions: pre-exposed to 1% CO/1.2% H_2O/Ar at 200 °C for 30 min, and finally exposed to 1.2% H_2O for 60 min).

promoting the consumption of the reactive intermediate acetate to produce CO. Subsequently, CO reacted with H_2O *via* the WGS reaction, generating CO_2 and abundant H_2.

The mechanism of the WGS reaction on Rh–Ce/Al_2O_3 catalysts was further investigated by TPSR experiments. On Rh–Ce_5/Al_2O_3, CO adsorption peaks (2083 cm^{-1} and 2012 cm^{-1}) were observed at 200 °C (Fig. 6a).[61–63] As the temperature increased, CO was rapidly consumed, while the amount of formate species (1590 cm^{-1}) increased and then decreased, indicating that formate species were the reactive intermediates during the WGS reaction. Meanwhile, the generation of H_2 and CO_2 was gradually increased at around 250 °C (Fig. 6b). Besides, less CO adsorption was observed on Rh/Al_2O_3 at 200 °C, and a small amount of formate species was generated as the temperature increased to 400 °C (Fig. S20a†). As the temperature further increased, CO and formate species were gradually consumed, with slight production of H_2 and CO_2 emerging at around 300 °C (Fig. S20b†). These findings indicated that CO would react with OH species, possibly derived from water activation, to form formate, which was ultimately dehydrogenated to CO_2.[3,12,13,62] The high formate production observed on Rh–Ce_5/Al_2O_3 may be due to the Rh–O–Ce structure, which enhanced CO adsorption and water activation, thereby resulting in the excellent WGS performance of this catalyst. Meanwhile, as the temperature increased, the amount of formate species initially increased, peaking at around 350 °C, and then decreased (Fig. S21a†), which indicated that formate was an important intermediate in the WGS reaction. In addition, the generation of H_2 was analyzed by calculating the first-order derivative of the H_2 production (Fig. S21b†). The results show that the trend of H_2 production was similar to that of formate production, where the concentration of H_2 initially increased, peaking at 355

°C, and then decreased with increasing temperature. The strong correlation between the evolution of formate species and H_2 production confirmed that formate is a key intermediate in the WGS reaction. To elucidate the reactivity of formate, step-response experiments were conducted. When Rh–Ce_5/Al_2O_3 was exposed to a mixture of $CO/H_2O/Ar$ at 200 °C, adsorbed CO (2083, 2037, and 2012 cm^{-1}) and formate (1594 cm^{-1}) were observed (Fig. 6c). Subsequently, after the removal of CO, both adsorbed CO and formate were rapidly consumed within 10 min, while the concentrations of H_2 and CO_2 increased significantly during the first 3 min and then gradually decreased over the next 3 min (Fig. 6d). These results further indicated that the key reaction pathway of WGS involved the reactive formate, while its high reactivity towards water attributed to the strong water activation ability of Rh–O–Ce. Additionally, when exposed to $CO/H_2O/Ar$ at 200 °C, lower adsorption of CO and minimal formate were observed on Rh/Al_2O_3, while the formate exhibited poor reactivity toward H_2O to produce H_2 and CO_2 (Fig. S20†). H_2O-TPD and CO-TPD experiments were further conducted to investigate the adsorption capacity of H_2O and CO (Fig. S22†). During H_2O-TPD experiments, Rh–Ce_5/Al_2O_3 showed increased adsorption of H_2O, whose bending vibrations were at 1658 cm^{-1} and stretching vibrations were between 3200 and 3600 cm^{-1},[64] and a higher desorption temperature (146 °C) than Rh/Al_2O_3 (133 °C), indicating that the Rh–O–Ce structure enhanced the adsorption capacity of water. Similarly, during CO-TPD experiments, Rh–Ce_5/Al_2O_3 exhibited increased adsorption of CO species (2088 cm^{-1} and 2014 cm^{-1}) and a higher CO desorption temperature (192 °C) than Rh/Al_2O_3 (182 °C), indicating that the Rh–O–Ce structure also enhanced the adsorption capacity of CO. As a result, the Rh–O–Ce sites improved the adsorption capacity for both H_2O and CO, which can effectively promote the WGS reaction. These findings suggested that Rh–O–Ce significantly promoted the dissociation of water molecules, which further facilitated the conversion of CO to formate and the subsequent formation of CO_2 and H_2.[62] In conclusion, on the Rh–Ce_5/Al_2O_3 catalyst, large CeO_2 nanoparticles trapped single-atom Rh to promote the formation of the Rh–O–Ce structure, which enhanced the water activation and CO adsorption, and subsequently facilitated the formation of formate, thus significantly increasing the efficiency of the WGS.

The structural characterization confirmed that Rh species are present as Rh nanoclusters on Rh/Al_2O_3. On the Rh–Ce_1/Al_2O_3 catalyst, Ce species were highly dispersed on the surface of Al_2O_3 and did not significantly change the physical and chemical state of Rh species. As the Ce content increased further, Ce species gradually transition into CeO_2 nanoparticles, exhibiting a concomitant increase in particle size. These large CeO_2 nanoparticles trapped Rh species, facilitating the formation of single-atom Rh and constructing a stable Rh–O–Ce structure on the Rh–Ce_5/Al_2O_3 catalyst. The Rh–O–Ce structure promoted H_2 spillover, which potentially enhanced the H_2 transfer capability of the catalyst, and notably, the catalytic test results indicated that water activation is a critical factor in governing the H_2 production. Furthermore, the activity of Rh–Ce/Al_2O_3 catalysts in the WGS reaction affected the product distribution, while an enhanced WGS activity led to an increase in CO_2 production accompanied by an increase in H_2 production. The Rh–Ce_5/Al_2O_3 catalyst exhibited enhanced water activation ability and improved WGS activity, highlighting the role of the Rh–O–Ce structure in promoting both water activation and the reactivity in the WGS reaction.

In situ DRIFTS-MS experiments demonstrated the main reaction mechanism of ESR on Rh–Ce/A_2O_3 catalysts. Initially, the reaction began with ethanol adsorption and dissociation to form ethoxy species (CH_3CH_2O*), followed by stepwise dehydrogenation to produce acetaldehyde (CH_3CHO).[13] Simultaneously, water underwent activation, resulting in the generation of reactive OH species.[3] Subsequently, the reactive OH species interacted with acetaldehyde to form acetate (CH_3COO*), which then dehydrogenated to generate CO.[12] Afterwards, CO further reacted with H_2O *via* the WGS reaction, whereas CO combined with reactive OH species to form formate, which ultimately dehydrogenated to produce H_2 and CO_2.[65] Notably, H_2 was produced during the stepwise dehydrogenation. The Rh–O–Ce structure not only promoted the dehydrogenative decomposition of ethoxy and acetaldehyde but also significantly enhanced water activation to generate reactive OH species. These reactive OH species played a crucial role in both the formation of acetate intermediates and the subsequent consumption of acetate to produce abundant H_2 and CO for the subsequent WGS reaction. Furthermore, the enhancement of CO adsorption and water activation also promoted the formation and dehydrogenation of formate, directly improving the WGS reaction activity.[66] The WGS reaction played a crucial role in the ESR reaction, serving as the primary source of CO_2 and H_2. On Rh–Ce_5/Al_2O_3, this process follows the formate mechanism, with the dehydrogenation of formate leading to the production of CO_2. Significantly lower H_2 and CO_2 generation temperatures were observed over Rh–Ce_5/Al_2O_3 compared to Rh/Al_2O_3. This suggested that formate dehydrogenation is the rate-determining step of the Rh–Ce/Al_2O_3 catalyst in the ESR reaction. Interestingly, the Rh–O–Ce structure significantly enhanced H_2 spillover, which likely accelerates the rapid dehydrogenation of intermediates and enables the efficient transfer of hydrogen to produce H_2. These promoting effects highlighted the critical role of Rh–O–Ce as an important site in enhancing hydrogen production over the Rh–Ce_5/Al_2O_3 catalyst. Besides, since the decomposition of acetate produced negligible CH_4, CH_4 may originate from the direct decomposition of acetaldehyde, a process that also generates CO.[12]

The transition from Rh nanoclusters in Rh/Al_2O_3 to Rh–O–Ce single-atom sites in Rh–Ce_5/Al_2O_3 played a pivotal role in enhancing catalytic performance. These Rh–O–Ce single-

atom sites significantly improved the ability to activate water and facilitated the generation and consumption of reactive intermediates acetate and formate, thereby increasing the H_2 production. These findings revealed the mechanism by which the interaction between CeO_2 nanoparticles and Rh species enhanced the reactivity of ESR. Furthermore, the understanding of enhanced water activation and the improved conversion efficiency of active intermediates, driven by the formation of new active sites through the interaction between dopants and metals, also offers valuable insights into the mechanisms of other related catalytic reactions.

4. Conclusion

This study elucidates the structure–activity relationship and reaction mechanism of Ce-doped Rh/Al_2O_3 catalysts in enhancing the activity of the ethanol steam reforming reaction. As the Ce loading increases, Ce species gradually aggregated from highly dispersed Ce atoms to form CeO_2 nanoparticles. CeO_2 nanoparticles effectively trapped Rh species to form single-atom Rh, constructing the Rh–O–Ce sites. During the ESR reaction, ethanol underwent dissociative adsorption to form ethoxy species, which dehydrogenated to produce acetaldehyde. Acetaldehyde reacted with reactive OH to form acetate, which dehydrogenated to CO. Afterward, CO reacted with OH to form formate, which decomposed to produce H_2 and CO_2. The Rh–O–Ce sites significantly promoted water activation, facilitating the generation of reactive OH species. Additionally, the Rh–O–Ce sites enhanced CO adsorption, accelerating its conversion to form formate *via* the water–gas shift reaction. This dual functionality increased the overall efficiency of $Rh–Ce/Al_2O_3$ in the ethanol steam reforming reaction. In conclusion, this work provides valuable insights into the mechanism of ethanol steam reforming on Ce-promoted Rh-based catalysts, offering guidance for high-efficiency catalysts.

Data availability

The data supporting this article have been included as part of the ESI.†

Author contributions

Lin Zhao: data curation, investigation, writing – original draft, review & editing. Diru Liu: data curation, investigation, writing – original draft, review & editing. Yiying Wang: investigation. Mengyuan Zhang: investigation. Qiang Wang: writing – review & editing, supervision. Guangyan Xu: conceptualization, methodology, validation, writing – review & editing, project administration, supervision. Hong He: writing – review & editing, supervision.

Conflicts of interest

There are no conflicts to declare.

Acknowledgements

This work was supported by the National Natural Science Foundation of China (22422609, 52225003), the Strategic Priority Research Program of the Chinese Academy of Sciences (XDA0390103), and the Project of Eco-environmental Technology for Carbon Neutrality (RCEES-TDZ-2021-6).

References

1 W. Shi, R. Zhang, H. Li, Y. Wu, S. Toan, Z. Sun and Z. Sun, *Adv. Energy Mater.*, 2023, **13**, 2301920.
2 H. Tian, C. Pei, Y. Wu, S. Chen, Z.-J. Zhao and J. Gong, *Appl. Catal., B*, 2021, **293**, 120178.
3 H. Meng, Y. Yang, T. Shen, W. Liu, L. Wang, P. Yin, Z. Ren, Y. Niu, B. Zhang, L. Zheng, H. Yan, J. Zhang, F.-S. Xiao, M. Wei and X. Duan, *Nat. Commun.*, 2023, **14**, 3189.
4 Y. Wu, C. Pei, H. Tian, T. Liu, X. Zhang, S. Chen, Q. Xiao, X. Wang and J. Gong, *JACS Au*, 2021, **1**, 1459–1470.
5 D. Zanchet, J. B. O. Santos, S. Damyanova, J. M. R. Gallo and J. M. C. Bueno, *ACS Catal.*, 2015, **5**, 3841–3863.
6 N. Artrith, Z. Lin and J. G. Chen, *ACS Catal.*, 2020, **10**, 9438–9444.
7 S. Crowley and M. J. Castaldi, *Angew. Chem., Int. Ed.*, 2016, **55**, 10650–10655.
8 Z. Ferencz, A. Erdőhelyi, K. Baán, A. Oszkó, L. Óvári, Z. Kónya, C. Papp, H. P. Steinrück and J. Kiss, *ACS Catal.*, 2014, **4**, 1205–1218.
9 T. Hou, S. Zhang, Y. Chen, D. Wang and W. Cai, *Renewable Sustainable Energy Rev.*, 2015, **44**, 132–148.
10 H. Wu and B. Yang, *Appl. Surf. Sci.*, 2023, **614**, 156116.
11 A. H. Martínez, E. Lopez, S. Larrégola, O. Furlong, M. S. Nazzarro, L. E. Cadús and F. N. Agüero, *Mater. Today Chem.*, 2022, **26**, 101077.
12 L. V. Mattos, G. Jacobs, B. H. Davis and F. B. Noronha, *Chem. Rev.*, 2012, **112**, 4094–4123.
13 D. Li, X. Li and J. Gong, *Chem. Rev.*, 2016, **116**, 11529–11653.
14 Y. C. Sharma, A. Kumar, R. Prasad and S. N. Upadhyay, *Renewable Sustainable Energy Rev.*, 2017, **74**, 89–103.
15 A. N. T. Cao, K. H. Ng, S. F. Ahmed, H. T. Nguyen, P. S. Kumar, H.-T. Tran, N. Rajamohan, M. Yusuf, P. L. Show, A. Balakrishnan, M. B. Bahari, T. J. Siang and D.-V. N. Vo, *Environ. Chem. Lett.*, 2024, **22**, 561–583.
16 S. Roychowdhury, M. M. Ali, S. Dhua, T. Sundararajan and G. R. Rao, *Int. J. Hydrogen Energy*, 2021, **46**, 19254–19269.
17 G. N. Radael, V. Martinelli and R. M. Pontes, *Theor. Chem. Acc.*, 2022, **141**, 13.
18 Z. Pu, H. Yin, X. Ma, J. Zhao and J. Zeng, *Chin. J. Catal.*, 2023, **48**, 247–257.
19 S.-i. Ito and S. Kameoka, *Appl. Catal., A*, 2021, **617**, 118113.
20 A. S. Asundi, A. S. Hoffman, P. Bothra, A. Boubnov, F. D. Vila, N. Yang, J. A. Singh, L. Zeng, J. A. Raiford, F. Abild-

Pedersen, S. R. Bare and S. F. Bent, *J. Am. Chem. Soc.*, 2019, **141**, 19655–19668.
21 X. Huang, D. Teschner, M. Dimitrakopoulou, A. Fedorov, B. Frank, R. Kraehnert, F. Rosowski, H. Kaiser, S. Schunk, C. Kuretschka, R. Schlögl, M.-G. Willinger and A. Trunschke, *Angew. Chem., Int. Ed.*, 2019, **58**, 8709–8713.
22 S. Lee, A. Patra, P. Christopher, D. G. Vlachos and S. Caratzoulas, *ACS Catal.*, 2021, **11**, 9506–9518.
23 J. Xiong, L. Tian and R. Cheng, *J. Hazard. Mater.*, 2021, **416**, 125913.
24 P. Osorio-Vargas, C. H. Campos, R. M. Navarro, J. L. G. Fierro and P. Reyes, *J. Mol. Catal. A: Chem.*, 2015, **407**, 169–181.
25 R. B. Duarte, O. V. Safonova, F. Krumeich, M. Makosch and J. A. van Bokhoven, *ACS Catal.*, 2013, **3**, 1956–1964.
26 C. Zhu, K. Xu, Y. Fang, Q. Lv, K. Jiang, H. Zhao, Y. Chen, P. Wang, H. Yang, L. Wu, Y. Tang and L. Tan, *Fuel*, 2023, **334**, 126770.
27 D. Carta, T. Montini, M. F. Casula, M. Monai, S. Bullita, P. Fornasiero and A. Corrias, *J. Mater. Chem. A*, 2017, **5**, 20024–20034.
28 I. I. Soykal, H. Sohn, D. Singh, J. T. Miller and U. S. Ozkan, *ACS Catal.*, 2014, **4**, 585–592.
29 D. M. Meira, R. U. Ribeiro, O. Mathon, S. Pascarelli, J. M. C. Bueno and D. Zanchet, *Appl. Catal., B*, 2016, **197**, 73–85.
30 X. Chen, C. Qu, Y. Xiao, W. Wang, J. Zhang, X. Zheng and Q. Ye, *Catal. Today*, 2024, **434**, 114687.
31 G. Cavusoglu, D. Miao, H. Lichtenberg, H. W. P. Carvalho, H. Xu, A. Goldbach and J.-D. Grunwaldt, *Appl. Catal., A*, 2015, **504**, 381–390.
32 M. D. Zhurka, A. A. Lemonidou and P. N. Kechagiopoulos, *Catal. Today*, 2021, **368**, 161–172.
33 Z. Liu, G. Xu, L. Zeng, W. Shi, Y. Wang, Y. Sun, Y. Yu and H. He, *Appl. Catal., B*, 2023, **324**, 122259.
34 Y. Sun, G. Xu, Y. Wang, W. Shi, Y. Yu and H. He, *Environ. Sci. Technol.*, 2023, **57**, 20370–20379.
35 Q. An, G. Xu, J. Liu, Y. Wang, Y. Yu and H. He, *ACS Catal.*, 2023, **13**, 6851–6861.
36 J. Ao, T. Wang, B. Zhang, S. Liu and G. Liu, *Int. J. Hydrogen Energy*, 2022, **47**, 25471–25485.
37 X. Cheng, X. Zhang, D. Su, Z. Wang, J. Chang and C. Ma, *Appl. Catal., B*, 2018, **239**, 485–501.
38 W. Wang, S. Song, P. Wang, M. He, Z. Fang, X. Yuan, H. Li, C. Li, X. Wang, Y. Wei, W. Song, H. Xu and Z. Li, *ACS Catal.*, 2023, **13**, 4597–4610.
39 J. C. Matsubu, V. N. Yang and P. Christopher, *J. Am. Chem. Soc.*, 2015, **137**, 3076–3084.
40 D. Wu, S. Liu, M. Zhong, J. Zhao, C. Du, Y. Yang, Y. Sun, J. Lin, S. Wan, S. Wang, J. Huang, Y. Yao, Z. Li and H. Xiong, *ACS Catal.*, 2022, **12**, 12253–12267.
41 P. Osorio-Vargas, C. H. Campos, R. M. Navarro, J. L. G. Fierro and P. Reyes, *Appl. Catal., A*, 2015, **505**, 159–172.
42 J. Wu, L.-Y. Qiao, Z.-F. Zhou, G.-J. Cui, S.-S. Zong, D.-J. Xu, R.-P. Ye, R.-P. Chen, R. Si and Y.-G. Yao, *ACS Catal.*, 2019, **9**, 932–945.
43 Z. Sun, S. Yu, S. Toan, R. Abiev, M. Fan and Z. Sun, *ACS Catal.*, 2023, **13**, 13704–13716.
44 P. Gao, G. Liang, T. Ru, X. Liu, H. Qi, A. Wang and F.-E. Chen, *Nat. Commun.*, 2021, **12**, 4698.
45 S. Bai, F. Liu, B. Huang, F. Li, H. Lin, T. Wu, M. Sun, J. Wu, Q. Shao, Y. Xu and X. Huang, *Nat. Commun.*, 2020, **11**, 954.
46 I. V. Yentekakis, G. Goula, M. Hatzisymeon, I. Betsi-Argyropoulou, G. Botzolaki, K. Kousi, D. I. Kondarides, M. J. Taylor, C. M. A. Parlett, A. Osatiashtiani, G. Kyriakou, J. P. Holgado and R. M. Lambert, *Appl. Catal., B*, 2019, **243**, 490–501.
47 B. Liu, N. Huang, Y. Wang, X. Lan and T. Wang, *ACS Catal.*, 2021, **11**, 1787–1796.
48 R. C. Rabelo-Neto, H. B. E. Sales, C. V. M. Inocêncio, E. Varga, A. Oszko, A. Erdohelyi, F. B. Noronha and L. V. Mattos, *Appl. Catal., B*, 2018, **221**, 349–361.
49 B. Liu, C. Li, G. Zhang, X. Yao, S. S. C. Chuang and Z. Li, *ACS Catal.*, 2018, **8**, 10446–10456.
50 M. Tóth, E. Varga, A. Oszkó, K. Baán, J. Kiss and A. Erdőhelyi, *J. Mol. Catal. A: Chem.*, 2016, **411**, 377–387.
51 J. Carrasco, D. López-Durán, Z. Liu, T. Duchoň, J. Evans, S. D. Senanayake, E. J. Crumlin, V. Matolín, J. A. Rodríguez and M. V. Ganduglia-Pirovano, *Angew. Chem., Int. Ed.*, 2015, **54**, 3917–3921.
52 M. Z. Granlund, K. Jansson, M. Nilsson, J. Dawody and L. J. Pettersson, *Appl. Catal., B*, 2014, **154–155**, 386–394.
53 Y. Zheng, K. Li, H. Wang, D. Tian, Y. Wang, X. Zhu, Y. Wei, M. Zheng and Y. Luo, *Appl. Catal., B*, 2017, **202**, 51–63.
54 S. Jin, D. Ye, T. Zhang, L. Lv, W. Tang, Y. Wang, Z. Zou and S. Tang, *Chem. Eng. J.*, 2025, **509**, 161198.
55 S. D. Davidson, J. Sun and Y. Wang, *Catal. Today*, 2016, **269**, 140–147.
56 C. Sun, S. Xiao, C. Jin, R. Ye, R. Zhang, L. Cheng, Q. Li and G. Feng, *J. Mater. Chem. A*, 2024, **12**, 16200–16209.
57 S. Y. Kim, M. Wang, H. Nguyen-Phu, D. H. Jeong and E. W. Shin, *J. Catal.*, 2022, **416**, 240–252.
58 T. S. Moraes, R. C. R. Neto, M. C. Ribeiro, L. V. Mattos, M. Kourtelesis, S. Ladas, X. Verykios and F. B. Noronha, *Appl. Catal., B*, 2016, **181**, 754–768.
59 M. Kourtelesis, T. S. Moraes, L. V. Mattos, D. K. Niakolas, F. B. Noronha and X. Verykios, *Appl. Catal., B*, 2021, **284**, 119757.
60 S. M. de Lima, I. O. da Cruz, G. Jacobs, B. H. Davis, L. V. Mattos and F. B. Noronha, *J. Catal.*, 2008, **257**, 356–368.
61 S. Xia, L. Fang, Y. Meng, X. Zhang, L. Zhang, C. Yang and Z. Ni, *Appl. Catal., B*, 2020, **272**, 118949.
62 L. Zhou, Y. Liu, S. Liu, H. Zhang, X. Wu, R. Shen, T. Liu, J. Gao, K. Sun, B. Li and J. Jiang, *J. Energy Chem.*, 2023, **83**, 363–396.
63 K. Larmier, W.-C. Liao, S. Tada, E. Lam, R. Verel, A. Bansode, A. Urakawa, A. Comas-Vives and C. Copéret, *Angew. Chem., Int. Ed.*, 2017, **56**, 2318–2323.
64 R. Gui, C. Zhang, Y. Gao, Q. Wang and A. M. Efstathiou, *Appl. Catal., B*, 2025, **361**, 124611.
65 D. B. Pal, R. Chand, S. N. Upadhyay and P. K. Mishra, *Renewable Sustainable Energy Rev.*, 2018, **93**, 549–565.
66 J. Vecchietti, A. Bonivardi, W. Xu, D. Stacchiola, J. J. Delgado, M. Calatayud and S. E. Collins, *ACS Catal.*, 2014, **4**, 2088–2096.